

1
2
3
4
5
6
7
8
9
10
11
12
13
14
15
16
17
18
19
20
21
22
23
24
25
26
27
28
29
30
31

Organ sculpting by patterned extracellular matrix stiffness

Justin Crest¹, Alba Diz-Muñoz^{2,§}, Dong-Yuan Chen¹, Daniel A. Fletcher², and David Bilder^{1*}

Affiliations:

¹Department of Molecular and Cell Biology, University of California-Berkeley, Berkeley CA, 94720, USA
and

²Department of Bioengineering & Biophysics Program, University of California-Berkeley, Berkeley CA, 94720, USA

[§]Current address: Cell Biology and Biophysics Unit, European Molecular Biology Laboratory, Heidelberg, 69117, Germany.

*Correspondence: bilder@berkeley.edu

SUMMARY

How organ-shaping mechanical imbalances are generated is a central question of morphogenesis, with existing paradigms focusing on asymmetric force generation within cells. We show here that organs can be sculpted instead by patterning anisotropic resistance within their extracellular matrix (ECM). Using direct biophysical measurements of elongating *Drosophila* egg chambers, we document robust mechanical anisotropy in the ECM-based basement membrane (BM) but not the underlying epithelium. Atomic force microscopy (AFM) on wild-type BM *in vivo* reveals an A-P symmetric stiffness gradient, which fails to develop in elongation-defective mutants. Genetic manipulation shows that the BM is instructive for tissue elongation and the determinant is relative rather than absolute stiffness, creating differential resistance to isotropic tissue expansion. The stiffness gradient requires morphogen-like signaling to regulate BM incorporation, as well as planar-polarized organization to homogenize it circumferentially. Our results demonstrate how fine mechanical patterning in the ECM can guide cells to shape an organ.

INTRODUCTION

Animal organs have a bewildering variety of distinctive forms that are critical for their functions. While originating in a genetic program, morphogenesis of organs ultimately depends on physical forces, and specifically their imbalances, to drive shape change (Thompson, 1917). A central question of morphogenesis is how such force imbalances are created by mechanical anisotropy that is generated within an organ's components. Current paradigms derive from archetypes of morphogenetic processes such as tissue elongation, and elegant studies have revealed conserved mechanisms that drive elongation across many species. In the *Drosophila* embryo, planar cell polarized (PCP) myosin contractility at the cell cortex generates junctional rearrangements that extend the germband, while in vertebrate embryos, PCP actin-based protrusions drive cell movements that extend the neural plate (Guillot and Lecuit, 2013; Heisenberg and Bellaiche, 2013; Vichas and Zallen, 2011; Walck-Shannon and Hardin, 2014). In these

textbook examples of morphogenesis, as in others such as gastrulation and epiboly, the force anisotropies that instruct shape are generated within the tissue's cells.

In theory, asymmetric organs could be generated not only by spatially-varying forces produced within cells, but also by spatially-varying tissue properties that differentially resist uniformly applied forces. In epithelial organs, morphogenetic forces include not only tension between cells that can cause intercellular rearrangements, but also expansion of luminal contents normal to the epithelial plane; resistance to these forces is mediated by cells and the extracellular matrix (ECM), including the basement membranes (BMs) that line all epithelia. In comparison to cellular forces, the role of non-cellular influences on morphogenesis is poorly understood.

A comprehensive study of morphogenetic mechanics requires a tissue subject to both cellular and extracellular influences. The *Drosophila* egg chamber (or 'follicle') is such a tissue (**Fig. 1A and Fig. 1- Fig. Supplement 1**) and undergoes robust elongation during its development (Spradling, 1993). Each follicle is a simple tube-like organ consisting of just two cell types, with a somatic epithelium of 'follicle cells' (FCs) encasing an interconnected cyst of germ cells; the epithelium also produces an underlying BM that surrounds the entire follicle. The organ is initially spherical and grows throughout oogenesis, expanding ~5000-fold in volume over ~3 days. Expansion for the first 35 hours is isotropic but subsequently becomes anisotropic, as the follicle elongates >2 fold specifically along the anterior-posterior (A-P) axis to form the distinctively shaped oval egg (**Fig. 1A**); much of this elongation takes place without cell division. Genes and cell behaviors that are required for egg elongation have been identified, but the mechanical environment that actually shapes the tissue is not known (Bilder and Haigo, 2012; Cetera and Horne-Badovinac, 2015).

Here we use biophysical tools to measure the mechanical conditions present in elongating follicles. Surprisingly, we find no evidence for differential cell-intrinsic forces within the organ, but instead document a robust spatial gradient in stiffness within the BM. Direct BM manipulation indicates that this mechanical gradient is instructive for tissue elongation. Fine mechanical patterning within the BM, generated by independent mechanisms along both the A-P and circumferential axes, endows the BM with

anisotropic resistance to tissue expansion that deforms the growing tissue. These results highlight a new parameter of developmental mechanics by uncovering an unappreciated sophistication in BM mechanical properties which can directly impose organ shape.

RESULTS

Cells in elongating follicles are mechanically isotropic

To understand the conditions that drive elongation of the *Drosophila* follicle, we first searched for mechanical anisotropy in the organ's two distinct cell populations. In these assays as well as others below, we examined follicles at st. 8 and earlier, when they display a regular and A-P symmetric morphology. Previous genetic mosaic experiments with several 'round egg' mutations exclude the germline as a site of action {Frydman:2001vk, Wieschaus:1981up, Viktorinova:2009in}, while stripping of epithelium in *Heteropeza* results in round rather than elongated follicles {Went:1981fs}. Similarly, we genetically ablated the *Drosophila* follicle epithelium (as well as its underlying BM), and found that germline growth resulted in a nearly spherical follicle at stages when elongation would normally have initiated (**Fig. 1- Fig. Supplement 1**). Together, these data suggest that the germline is not an intrinsic source of mechanical anisotropy.

To assess whether the follicle epithelium showed PCP cortical contractility, we laser-ablated cellular junctions at different positions along the A-P axis and measured the recoil. In elongating epithelia including the *Drosophila* ectoderm and wing, this technique reveals differential tension along A-P and D-V axes, an anisotropy associated with polarized Myosin II accumulation (Bosveld et al., 2012; Etournay et al., 2015; Fernandez-Gonzalez et al., 2009; Rauzi et al., 2008). However, in the elongating follicle epithelium, dissection of junctions resulted in equivalent retraction of A-P and circumferentially-oriented junctions; polarized accumulation of Myo:GFP was also not observed (**Fig. 1-Fig. Supplement 1**). These results suggest that neither cell type of the follicle intrinsically generates anisotropic physical forces.

Patterned mechanical stiffness in the follicle BM

To identify the source of mechanical anisotropy, we therefore turned to a non-cellular component of the organ: the ECM, specifically the BM. The *Drosophila* follicle is enclosed by a BM that, like classic vertebrate BMs, is ~150 nm thick and contains Collagen IV, Laminin, and Perlecan (Haigo and Bilder, 2011; Isabella and Horne-Badovinac, 2015; Spradling, 1993). BMs and surrounding ECM are known to have important influences on animal organogenesis (Daley and Yamada, 2013; Morrissey and Sherwood, 2015), but understanding their mechanical roles has been impeded by the difficulty of measuring these directly *in vivo*. In the *Drosophila* follicle, the external position of the BM, the absence of a cellular stroma (**Figs. 1A and Fig. 1- Fig. Supplement 1**), and the ability to develop in culture provided an unprecedented opportunity to assess the mechanical properties of an intact BM, in living tissue under physiological conditions.

We utilized Atomic Force Microscopy (AFM) to measure BM stiffness, calculating the Young's modulus from the deflection of a cantilevered probe indenting (**Fig. 1B, C, Fig. 1- Fig. Supplement 2**) into the basal follicle surface. Treatment of follicles with purified Collagenase decreased stiffness by 97% without detectable changes to epithelial junctions, while disruption of the cellular actomyosin network with Latrunculin A induced no significant change in AFM measurements. Furthermore, reducing the turgor pressure of the follicle with a hypertonic solution (2000mOsm Sorbitol media) does not have an effect on the BM stiffness (**Fig. 1D and Fig. 1- Fig. Supplement 3**). These controls indicate that the quantified stiffness predominantly derives from the BM.

AFM measurements at the center of staged wild-type (WT) follicles showed that the BM gradually stiffens as oogenesis proceeds, increasing from ~30 KPa at stage 3 to ~40 KPa at stage 5 and ~70 KPa at stage 7 (**Fig. 1D**). Interestingly, although stiffness was highly consistent (>5% variance) around the circumferential axis at a given position (**Fig. 4N**), it significantly varied along the A-P axis (**Fig. 1E**). At stages 3 and 5, poles were ~50% softer than the central or terminal regions (see **Fig. 1D** for definitions). This difference persisted into later stages, and the central regions further became ~30% more stiff than the terminal regions. Thus, AFM analysis reveals a symmetrical gradient of BM stiffness along the A-P axis of the follicle.

BM stiffness is instructive for tissue elongation

If the BM stiffness gradient is functionally important for organ elongation, it should be perturbed in conditions where elongation fails. We analyzed two distinct genotypes in which follicle elongation is defective: mutants for *fat2*, which encodes an atypical cadherin that controls basal PCP organization in the follicle epithelium (Viktorinova et al., 2009), and RNAi depleting *misshapen (msn)*, which encodes a kinase that negatively regulates integrin-mediated adhesion (Lewellyn et al., 2013). We carried out AFM on staged *fat2* follicles and found that, unlike WT, BM stiffness did not increase from stage 5 to stage 7 (**Fig. 1F**). Strikingly, *fat2* follicles showed no significant differences between the central, terminal, and polar regions at either stage. An isotropic and softer BM was also seen in *msn*-depleted follicles, despite their elevated integrin levels (Lewellyn et al., 2013)(**Fig. 1F**). The lack of a BM stiffness gradient in non-elongating follicles is consistent with this mechanical property playing an important role in organ elongation.

The above data suggest the hypothesis that BM stiffness is in fact the anisotropic mechanical property that drives organ shape, deforming the growing tissue. An alternative is that BM stiffness is instead an indirect consequence of organ shape, passively reflecting undetected changes in cell-intrinsic properties. To distinguish between these possibilities, we directly manipulated BM components. We then measured effects on BM mechanics and subsequent tissue elongation, including manipulations where the A-P stiffness gradient was either eliminated or preserved. The follicle epithelium produces most of its own BM, which can be altered by follicle-wide RNAi or overexpression driven by *tj-Gal4* (**Fig. 2I**) (Haigo and Bilder, 2011; Isabella and Horne-Badovinac, 2015; Van De Bor et al., 2015). AFM measurements on follicles depleted for SPARC, a factor involved in early BM incorporation of Collagen IV, showed that BM stiffness was ~80% of WT in the central regions, but preserved a gradient with increased elasticity at both terminal regions and poles; elongation of these follicles was indistinguishable from WT (**Fig. 2A, B**) (Isabella and Horne-Badovinac, 2015; Martinek et al., 2008; Pastor-Pareja and Xu, 2011). This is distinct from follicles uniformly

depleted of Collagen IV, which are homogenously soft and are defective in elongation, resembling *fat2* and *msn*-depleted follicles (**Figs. 2C-E**) (Haigo and Bilder, 2011; Isabella and Horne-Badovinac, 2015). In contrast, uniform overexpression of EHBP1, which elevates Collagen IV fibril deposition, leads to ~15% increased central stiffness with a ~20% increased anisotropic gradient, and results in organ hyperelongation (**Fig. 2F**) (Isabella and Horne-Badovinac, 2016).

We then turned to spatially restricted GAL4 drivers that allow manipulation of BM components in subsets of the gradient. We depleted Collagen IV specifically in the central FCs (using *mirr-GAL4*, **Fig. 2J**), where BM stiffness is normally maximal. AFM measurements showed that this manipulation eliminated stiffness differences between the central and terminal regions, and these follicles show significant elongation defects (**Fig. 2G**). To complement this manipulation, we overexpressed EHBP1 locally in the terminal regions (using *fru-GAL4*, **Fig. 2K**). This also equilibrated stiffness between the central and terminal regions, and again led to rounder follicles (**Fig. 2H**). The data overall (**Fig. 2L**) indicate that a spatially-varying gradient in BM stiffness is essential for elongation, with absolute BM stiffness playing a lesser role. Importantly, direct manipulation of AFM-measured BM stiffness, with predictable changes to follicle morphogenesis, argues that the stiffness gradient is instructive for organ shape.

Anisotropic resistance to tissue expansion by the mechanically patterned BM

To functionally test whether soft or stiff, and isotropic or anisotropic BMs can indeed resist tissue expansion differentially, we adapted an organ swelling assay (Pastor-Pareja and Xu, 2011). We immersed live follicles in deionized water, creating osmotic stress that leads to water influx into the follicle (**Fig. 3A, B, Video 1**). Acute expansion of the organ challenges the BM, resulting in bursting which can be monitored by live imaging. This assay measures BM rather than epithelial failure, since the follicle epithelium is disrupted well prior to bursting and Latrunculin A treatment does not accelerate bursting (**Fig. 3C, D**). We hypothesized that the frequency and speed at which the BM bursts would reflect its overall stiffness, whereas the position where it burst could indicate the location of a weak point. Consistent with the former hypothesis,

WT follicles at st. 8 were more resistant to bursting than at stage 5 (**Fig. 3C, D**). All collagenase-treated follicles burst instantly. Uniformly depleting Collagen IV or SPARC also induced strong increases in bursting frequency, while depleting Collagen IV in the central FCs alone did not (**Fig. 3F**). *Fat2* and *msn*-depleted follicles showed a phenotype similar to that of directly weakening the BM, and burst more frequently and rapidly compared to WT (**Fig. 3C, D, F; Video 2, 4**), whereas EHBP1-overexpressing follicles were completely resistant to bursting (**Fig. 3F; Video 4**). Consistent with the latter hypothesis, WT follicles burst most frequently at polar regions, while bursting in collagenase-treated follicles showed no such preference, and *fat2* follicles burst more frequently than WT in non-polar regions (**Fig. 3E**). Other BM manipulations also showed bursting phenotypes consistent with the hypothesis (**Fig. 3F, G**). For instance, depletion of Collagen IV in the central FCs (*Mirr>ColIV^{KD}*) relocalized swelling and bursting to this region (**Video 4**). Soft follicles in general burst more frequently and more rapidly, whereas mechanically isotropic follicles swelled more isotropically before bursting (**Fig. 3F, G**). Overall, the organ swelling experiments support the hypothesis that the WT gradient in BM stiffness provides differential resistance to organ expansion that is highest along the central meridian, and lowest at the poles where most elongation occurs.

Circumferential patterning of the stiffness ‘corset’

In what elements does the stiffness gradient lie, and how is it generated? Previous work has suggested that the follicle is shaped by a ‘molecular corset’, resulting from the PCP organization of cytoskeletal elements or BM fibril-like structures (Bilder and Haigo, 2012; Cetera and Horne-Badovinac, 2015; Gutzeit et al., 1993; Isabella and Horne-Badovinac, 2016; Tucker and Meats, 1976). We used the ‘tissue flattening’ image analysis tool ImSAnE (Heemskerk and Streichan, 2015; Lipari et al., 2016) to comprehensively analyze follicle BM, including around the entire A-P and circumferential axes of the organ (**Fig. 4A**). In addition to PCP fibril organization, this approach revealed two unappreciated features.

First, around the circumferential axis, ImSAnE showed that WT follicles display a fairly uniform distribution of Collagen IV fibrils, suggesting a regular supracellular network. By contrast, in *fat2* follicles, ImSAnE documented not only the loss of BM fibril polarity, but also revealed discontinuous and variable distribution of Collagen IV, with regions of high and low deposition (**Fig. 4B-D**). These phenotypes were shared by follicles depleted for *msn*. Strikingly, in both *fat2* and *msn*-depleted follicles, AFM measurements around the circumference at a single A-P position (**Fig. 4E**) revealed a four-fold increase in variability of stiffness, compared to the highly consistent stiffness of WT follicles (**Fig. 4F**). The data raise the possibility that uniform circumferential mechanical properties, dependent on tissue rotation, may also be required for elongation.

Morphogen-like signaling induces the organ-shaping AP mechanical gradient

Second, along the AP axis, we noted intriguing A-P differences in BM component levels. During elongation, Collagen IV levels are increased in central regions and taper toward the poles (**Fig. 5A**). Perlecan levels by contrast are lower at anterior and central regions than elsewhere (**Fig. 5B**). Finally, Laminin levels are fairly uniform but are low at the anterior (**Fig. 5C**). We extended the analysis of Collagen IV, which is a major contributor to BM stiffness (Morrissey and Sherwood, 2015). Quantitation using ImSAnE documented a significant increase of Collagen IV levels in central as compared to anterior and posterior terminal regions (**Fig. 5H, I**). This pattern is not solely transcriptional, as Collagen IV subunit gene expression is not elevated in the central region (Van De Bor et al., 2015) (**Fig. 5F**), and uniform ectopic expression of Collagen IV subunits (via 'FLPout GAL4') results in non-uniform incorporation into the BM, enhanced in the follicle center (**Fig. 5G**).

We investigated how these A-P differences in BM composition are regulated. Regional variance in BM stiffness will result from a combination of transcriptional and post-transcriptional regulation (including secretion, incorporation, and higher order modification) of Collagen IV along with other BM components. We asked whether any of these processes are controlled by an organizer-like activity that exists at the follicle poles, in which secretion of a cytokine signal activates JAK/STAT to distinguish cell

fates along the A-P axis (Xi et al., 2003). Interestingly, inhibition of JAK/STAT signaling (via expression of a dominant negative receptor) eliminated the differential A-P distribution of Collagen IV without affecting fibril polarity, and this manipulation gave rise to round follicles and eggs (**Figs. 4B, 5J**). Importantly, AFM measurements demonstrated that these follicles showed relatively high but isotropic BM stiffness (**Fig. 5K**). We conclude that morphogen-like signaling results in BM mechanical patterning to drive elongation.

How do the various mechanical properties described above integrate to shape the organ? ‘Molecular corset’ models derive in part from analysis of follicles mutant for *fat2*, the prototypical egg elongation regulator, and their mispolarization of PCP elements such as BM fibrils (**Fig. 4B**). However, *fat2* follicles also fail to achieve an even distribution of BM around the follicle circumference (**Fig. 4C, D**). Additionally, ImSAnE quantitation reveals that they have perturbed A-P Collagen IV pattern, although no changes in A-P signaling are seen (**Fig. 5H, I, Fig. 5- Fig. Supplement 2**). Finally, *fat2* follicles fail to undergo a whole-tissue rotation event associated with elongation (Haigo and Bilder, 2011; Viktorinová and Dahmann, 2013). To assess the role of active rotation, we depleted the actin regulator Abi at st. 5, which results in rotation arrest as elongation initiates (Cetera et al., 2014). These follicles stiffened comparably to WT, showed bursting response comparable to WT, and also elongated normally (**Fig. 5- Fig. 1- Fig. Supplement 3, Video 3**). Conversely, elongation is prevented without disrupting rotation in several genotypes (see below, **Video 3**), confirming that phenomena other than active rotation are required for follicle shape. Nevertheless, the altered tissue-wide distributions of Collagen IV in *fat2* complicate interpretations that BM fibril PCP forms the molecular corset.

We were unable to identify manipulations that independently disrupted follicle PCP and the circumferentially continuous BM distribution. Therefore, to investigate the role of BM fibril polarity per se in generating elongation-driving mechanical anisotropy, we uniformly overexpressed Perlecan, which antagonizes constrictive properties of Collagen IV BMs and can induce round eggs (Isabella and Horne-Badovinac, 2015;

Pastor-Pareja and Xu, 2011). This manipulation did not change the A-P levels, PCP, or circumferential distribution of Collagen IV fibrils (**Fig. 4B, D, 5H, I**). However, AFM analysis revealed that it created a softer BM in which the anisotropic gradient has been eliminated, and the enclosed follicles fail to elongate (**Fig. 5J, K**). In osmotic stress experiments, follicles overexpressing Perlecan swelled more isotropically and burst more rapidly than WT (**Fig. 5L**). Thus, despite the fact that neither the levels, local PCP, or supracellular organization of Collagen IV fibrils are altered, the BM of Perlecan-overexpressing follicles had mechanical deficits similar to follicles completely lacking a BM. By contrast, follicles deficient for STAT-dependent A-P signaling also fail to elongate but show normal fibril polarity and organization, and are significantly more resistant to bursting (**Fig. 4B, 5J-L**). Together, these data support a requirement for a circumferentially even distribution of PCP fibrils in elongation. However, they also reveal that PCP fibrils are insufficient alone to anisotropically resist tissue growth; the organ-shaping stiffness gradient requires patterned A-P BM levels.

DISCUSSION

Organ elongation is a fundamental developmental process, and is generally considered to be driven by cell-intrinsic polarized mechanical forces that actively deform tissues. Here we demonstrate that an elongating tissue can rely instead on mechanical anisotropy patterned into the BM. Our data indicate that this asymmetric resistance within the extracellular environment, rather than asymmetric force generation within the cells, plays the dominant role in molding the follicle, prescribing subsequent morphogenetic cell behaviors. These results direct increased attention to fine BM spatial organization in creating the mechanical environment that shapes each tissue, and may fill the gap between the limited repertoire of cell-based morphogenetic mechanisms and the immense diversity of organ shapes.

Stromatic ECMs and BMs surround most animal organs, but their full roles in morphogenesis remain unresolved. Long regarded as an inert scaffold, ECM is known to influence tissue biology through actively regulating ligand availability and adhesion

signaling; local BM deposition and degradation also play key roles in branching morphogenesis of several mammalian organs (Daley and Yamada, 2013; Harunaga et al., 2014; Morrissey and Sherwood, 2015; Pastor-Pareja and Xu, 2011; Varner and Nelson, 2014). However, analysis of mechanical properties of vertebrate BMs *in vivo* is hampered by surrounding cellular stroma, whose removal necessitates non-physiological manipulations. Because of this, only exceptionally robust BMs such as those of the eye have been analyzed following denuding protocols (Ali et al., 2016). By contrast, fly follicles lack a cellular stroma, and their topology allows direct access of AFM probes to the BM of an intact, living tissue.

Our *in vivo* biophysical measurements of this native BM reveal an unappreciated degree of tissue-level mechanical patterning. Within each follicle, BM stiffness develops reliably and with spatial properties that are carefully regulated in both axes. Along the A-P axis, a stiffness gradient is built that increases ~300% along a ~13 cell, 100 μ m arc at st. 8. Perpendicular to this axis, stiffness around the circumference varies by less than 5% across the same distance. Data here reveal that both axes are critical for organ shaping, and merit a significant revision to the ‘molecular corset’ model previously proposed to mediate elongation (Bilder and Haigo, 2012; Cetera and Horne-Badovinac, 2015; Gutzeit et al., 1993; Isabella and Horne-Badovinac, 2016; Tucker and Meats, 1976). Hypotheses of corset structure have focused on the PCP organization of the basal actin network, the microtubule cytoskeleton, or the fibril-like BM. However, manipulations that preserve PCP alignment but nevertheless result in round follicles demonstrate that mechanical anisotropy at the length scale of individual BM fibrils is not sufficient to drive elongation. Instead, they suggest that consistent circumferential stiffness, likely associated with the supracellular BM fibrillar network generated by whole-tissue rotation, is a key element of corset effectiveness. Moreover, manipulations that flatten a pole-derived A-P signaling gradient also flatten the AP stiffness gradient, and create isotropic organs. Thus, to drive elongation, the corset must be anisotropic on a ‘global’ tissue-wide scale as well, in a manner that depends on morphogen-regulated mechanical properties.

The direct manipulations of BM components presented here, which lead to predicted outcomes on tissue shape, argue that BM mechanics themselves are instructive for morphogenesis. Flattening the stiffness gradient in several ways, including via locally restricted BM alteration, prevents elongation, whereas hyperelongating follicles have an enhanced stiffness gradient. Although we cannot rule out undetected roles of these manipulations in altering cell behaviors via classical intercellular signaling, we see no evidence for such changes in the underlying epithelium. Instead, our results indicate that elongation is imposed by isotropic tissue growth meeting the anisotropic resistance fashioned within the BM. Consistent with this model, manipulations that alter absolute stiffness but preserve a relative gradient still result in tissue elongation. The extent to which ovarian cells respond compliantly, or through well-characterized mechanical feedback mechanisms remain to be determined, but the data point to BM physical properties as the dominant influence.

Our results reveal a tissue elongation mechanism that is conceptually different from cell-intrinsic force asymmetries. Construction of mechanically patterned resistance in an ECM, along both axes orthogonal to its tissue interface, generates a force imbalance that imposes a specific shape on the growing organ, without necessitating spatially restricted localization of force generators within cells. Emerging examples point to the influence that substantial changes in exogenous physical forces can have in organ morphogenesis (Aigouy et al., 2010; Behrndt et al., 2012; Etournay et al., 2015; Harunaga et al., 2014; ray et al., 2015; Shyer et al., 2013) as well as in cancer (Kaushik et al., 2016). The discovery of precise organ-sculpting resistance within a BM motivates the development of tools and assays to explore, on a fine scale, true *in vivo* BM mechanical properties in both physiological and pathological contexts.

MATERIALS AND METHODS

Drosophila strains

GAL4 drivers used were *UAS-GAL4*, *mirrGAL4* and *fruGAL4* (Borensztein et al., 2013); *tubGAL80ts* was used to temporally control expression via shifting flies to 29°. The Drosophila genome contains two Collagen IV subunit-encoding genes: *CollV α 1* (Flybase: *Cg25c*) and *CollV α 2* (Flybase: *vkg*). For ease, both are referred to in the text and figures as Collagen IV; detailed genotypes for all experiments are listed in **Supplemental Table 1**. Overexpression constructs *UAS-DT-A*, *UAS-Perlecan* (Flybase: *Trol*), *UAS-DomeDN*, and *UAS-EHBP1* (Giagtzoglou et al., 2012); RNAi constructs against *Abi*, *SPARC*, *CollV α 1*, *CollV α 2*, *msn*; and GFP protein traps in Collagen IV α 2 and Perlecan were obtained from the Bloomington stock center. Fosmids carrying *LanB1-GFP* (Sarav et al., 2016) were obtained from VDRC; *Myo-GFP* (Flybase: *sqh*) was provided by Dan Kiehart. Ectopic expression of CollIV-GFP (*UAS-GFP-CollV α 1* + *UAS-GFP-CollV α 2*), provided by S. Noselli (Van De Bor et al., 2015), utilized *hsFLP*; *act>y+>GAL4*; *UAS-myrRFP*, activated by a 30' heat shock at 37° and immediately imaged with RFP signal to confirm uniform expression. *fat2^{KO}*, kindly provided by Mike Simon, is a null allele generated by ends-out gene replacement (Maggert et al., 2008) into the first exon and phenocopies other *fat2* null alleles (**Fig. 5- Fig. Supplement 1**).

Imaging and analysis

Ovary preparations for fixed and live imaging were performed as previously described (Lipari et al., 2016). Phalloidin-staining of fixed follicles used 20nM (Sigma). Latrunculin A 50 μ M (Sigma), FM4-64FX 5 μ g/mL (Thermo), and purified Collagenase 1000U/mL (Worthington LS005273) were diluted in Schneider's complete media (10mg/mL insulin, FBS and pen/strep) for live imaging. The measured osmolarity of the standard media was 300mOsm. Hypertonic shrinking was performed in standard media supplemented with 1M D-Sorbitol (Sigma) to 2000mOsm. Fixed follicles were mounted with tape spacers, except for flattened preparations which lacked spacers, and ImSAnE preparations which were mounted in a depression slide. Single-plane confocal images were acquired on a Zeiss LSM700 using a Plan Apochromat 20x/NA 0.8 lens or a LD C-

Apochromat 40x/NA 1.1 water-immersion lens and processed in Fiji (Schindelin et al., 2012). Representative images were isolated and assembled into figures using Adobe Photoshop and Illustrator CS6.

For cortical MyoII planar polarity quantification (Munjal et al., 2015), IMSAnE (Heemskerk and Streichan, 2015) was used to 'unroll' the follicle epithelia as previously described (Lipari et al., 2016) with modifications. Apical surface of interest (SOI) of the epithelia were identified by Sqh-GFP signal. Multilayered cylinder projections of the apical-lateral membranes from the apical most SOI plus minus 2-2.5 μ m were generated by IMSAnE class CylinderMeshWrapper. Maximum intensity projections were background subtracted with Fiji plugin 'subtract background'. A-P and circumferential junctions were categorized by 60-90° and 0-30° degrees relative to the A-P axis respectively. Cortical Sqh-GFP was selected manually with line tools (width 8px) on >30 junctions of each type; the mean ratio was plotted.

For CollV-GFP intensity measurements, *in toto* images were collected with pixel width of 0.17 μ m and voxel depth of 0.50 μ m without Z-intensity correction. Follicle SOI was identified using basal F-actin signal and generalized sinusoidal projections were generated by the IMSAnE class spherelikeFitter. Maximum intensity projection from multilayered pullbacks +/- 3 μ m from the basal epithelia were generated. To measure A-P intensity, 5 1px-wide lines were drawn within a 10 μ m wide stripe at the central meridian, where the pullbacks have minimal distortion; to measure circumferential intensity, 5 circumferential 1px-wide lines were drawn within a 10 μ m wide stripe along the circumferential meridian. Intensities were standardized to follicle length, then compared across follicles. Variance was calculated for each follicle using the Excel var.p formula. Profile plots were generated in Fiji.

Laser ablation

Ecad-GFP follicles were dissected in media and placed in a glass bottom dish. A pulsed Mai-Tai two-photon on a Zeiss LSM 510 confocal microscope was used to sever A-P or circumferential junctions at anterior, center, and posterior positions on the follicle.

At 708nm and 90% power the ablation time was less than 1 sec and the resulting junction relaxation distances were measured within 300ms. Analysis was executed manually in Fiji normalizing the relaxed distance to the original junction length. Similar results were obtained using a UV Micropoint laser at 50% power and a Nikon Ti-E inverted microscope with Yokogawa X1 confocal spinning disk head, with images continuously collected (500ms/frame).

Atomic Force Microscopy

BM stiffness was measured (**Fig 1- Fig. Supplement 2**) using either a Bruker Catalyst AFM controlled by Nanoscope 8.10 software or a custom built AFM controlled by LAbview software, both mounted on an inverted Zeiss AxioObserver Z1 microscope. MLCT-C cantilevers (Bruker) with a pyramidal tip and a nominal spring constant of 10 pN/nm were used in all experiments. The actual spring constant of each cantilever was determined by thermal calibration in air. Measurements were done in fluid. Approach velocity was optimized as 0.4 $\mu\text{m}/\text{sec}$ to ensure the fastest rate of elastic measurement without viscoelastic deformation. Sample rate of deflection was 2048. Retraction speed, which does not affect elasticity measurements, was set to 20 $\mu\text{m}/\text{sec}$. Follicles were prepared as for live imaging; the cantilever was positioned at the desired position by brightfield microscopy. Each positional measurement was taken 4 times without moving the cantilever in XY and averaged. Young's Modulus of elasticity was calculated by fitting the cantilever deflection versus piezo extension curves to the modified Hertz model as described (Rosenbluth et al., 2006), using a custom-written algorithm in MATLAB (Mathworks). Only the first 50nm of indentation were used to isolate elasticity from just the basement membrane. For pole measurements, PDMS egg holders were created using custom-made molds, coated first with poly-D lysine and then treated with complete growth media. Follicles were gently mounted in PBS which was subsequently replaced with media.

Osmotic swelling

Follicles dissected in complete media were adhered to poly-D lysine glass bottom dish (MatTek) before replacing media twice with dH₂O. Images were collected at 15 or 30 second intervals on a Zeiss Axioimager with Plan-Neofluor 10x/0.38NA objective.

Statistical Analysis

Data was analyzed and displayed using Microsoft Excel. All error bars represent standard error and centers represent mean. At least three biological replicates were done for each experiment and are stated in Supplementary file 1. All acquired data was included with the exception of the AFM experiments. For these, only follicles in which all three lateral positions could be quantified were used. Statistical analysis for all data used 2-tailed t-tests with p-value thresholds of *: $p < 0.05$, **: $p < 0.01$, ***: $p < 0.001$.

ACKNOWLEDGEMENTS

We thank Sebastian Streichan and Jan Liphardt for helpful discussions, Jessica Feldman for generously providing access to the laser ablation microscope, Sungmin Son and Andrew Harris for help with the AFM, and Mike Simon, Stephane Noselli, Hugo Bellen, Dan Kiehart, the Vienna Drosophila Resource Center, and the Bloomington Drosophila Stock Center (NIH P40OD018537) for reagents. J.C. is a Robert Black Fellow (DRG 2173-13) and A. D-M. is a Fellow (DRG 2157-12) of the Damon Runyon Cancer Research Foundation. This work was supported by NIH RO1s GM68675 and GM111111 to D.B, and GM074751 to D.A.F.

515

516

517 REFERENCES

- 518 Aigouy, B., Farhadifar, R., Staple, D.B., Sagner, A., Roper, J.C., Julicher, F., and Eaton,
519 S. (2010). Cell flow reorients the axis of planar polarity in the wing epithelium of
520 *Drosophila*. *Cell* 142, 773–786.
- 521 Ali, M., Raghunathan, V., Li, J.Y., Murphy, C.J., and Thomasy, S.M. (2016).
522 Biomechanical relationships between the corneal endothelium and Descemet's
523 membrane. *Exp. Eye Res.* 152, 57–70.
- 524 Behrndt, M., Salbreux, G., Campinho, P., Hauschild, R., Oswald, F., Roensch, J., Grill,
525 S.W., and Heisenberg, C.-P. (2012). Forces driving epithelial spreading in zebrafish
526 gastrulation. *Science* 338, 257–260.
- 527 Bilder, D., and Haigo, S.L. (2012). Expanding the morphogenetic repertoire:
528 perspectives from the *Drosophila* egg. *Dev Cell* 22, 12–23.
- 529 Borensztein, A., Boissoneau, E., Fernandez, G., Agnès, F., and Pret, A.-M. (2013).
530 JAK/STAT autocontrol of ligand-producing cell number through apoptosis. *Development*
531 140, 195–204.
- 532 Bosveld, F., Bonnet, I., Guirao, B., Tlili, S., Wang, Z., Petitalot, A., Marchand, R.,
533 Bardet, P.-L., Marcq, P., Graner, F., et al. (2012). Mechanical control of morphogenesis
534 by Fat/Dachsous/Four-jointed planar cell polarity pathway. *Science* 336, 724–727.
- 535 Cetera, M., and Horne-Badovinac, S. (2015). Round and round gets you somewhere:
536 collective cell migration and planar polarity in elongating *Drosophila* egg chambers.
537 *Curr. Opin. Genet. Dev.* 32, 10–15.
- 538 Cetera, M., Ramirez-San Juan, G.R., Oakes, P.W., Lewellyn, L., Fairchild, M.J.,
539 Tanentzapf, G., Gardel, M.L., and Horne-Badovinac, S. (2014). Epithelial rotation
540 promotes the global alignment of contractile actin bundles during *Drosophila* egg
541 chamber elongation. *Nature Communications* 5, 5511.
- 542 Chen, D.-Y., Lipari, K.R., Dehghan, Y., Streichan, S.J., and Bilder, D. (2016). Symmetry
543 Breaking in an Edgeless Epithelium by Fat2-Regulated Microtubule Polarity. *Cell*
544 *Reports* 15, 1125–1133.
- 545 Daley, W.P., and Yamada, K.M. (2013). ECM-modulated cellular dynamics as a driving
546 force for tissue morphogenesis. *Curr. Opin. Genet. Dev.* 23, 408–414.
- 547 Etournay, R., Popović, M., Merkel, M., Nandi, A., Blasse, C., Aigouy, B., Brandl, H.,
548 Myers, G., Salbreux, G., Jülicher, F., et al. (2015). Interplay of cell dynamics and
549 epithelial tension during morphogenesis of the *Drosophila* pupal wing. *eLife* 4, e07090.

550 Fernandez-Gonzalez, R., de Matos Simoes, S., Roper, J.C., Eaton, S., and Zallen, J.A.
 551 (2009). Myosin II Dynamics Are Regulated by Tension in Intercalating Cells. *Dev Cell*
 552 17, 736–743.

553 Giagtzoglou, N., Yamamoto, S., Zitserman, D., Graves, H.K., Schulze, K.L., Wang, H.,
 554 Klein, H., Roegiers, F., and Bellen, H.J. (2012). dEHBP1 controls exocytosis and
 555 recycling of Delta during asymmetric divisions. *J. Cell Biol.* 196, 65–83.

556 Guillot, C., and Lecuit, T. (2013). Mechanics of Epithelial Tissue Homeostasis and
 557 Morphogenesis. *Science* 340, 1185–1189.

558 Gutzeit, H.O., Vonseydlitzkurzbach, E., and Neuschroer, R. (1993). How *Drosophila*
 559 (Diptera, Drosophilidae) Follicles Become Spatially Organized and Obtain Their Ovoid
 560 Shape. *Int J Insect Morphol* 22, 335–347.

561 Haigo, S.L., and Bilder, D. (2011). Global tissue revolutions in a morphogenetic
 562 movement controlling elongation. *Science* 331, 1071–1074.

563 Harunaga, J.S., Doyle, A.D., and Yamada, K.M. (2014). Local and global dynamics of
 564 the basement membrane during branching morphogenesis require protease activity and
 565 actomyosin contractility. *Dev. Biol.* 394, 197–205.

566 Heemskerk, I., and Streichan, S.J. (2015). Tissue cartography: compressing bio-image
 567 data by dimensional reduction. *Nature Methods* 12, 1139–1142.

568 Heisenberg, C.P., and Bellaiche, Y. (2013). Forces in Tissue Morphogenesis and
 569 Patterning. *Cell* 153, 948–962.

570 Isabella, A.J., and Horne-Badovinac, S. (2015). Dynamic regulation of basement
 571 membrane protein levels promotes egg chamber elongation in *Drosophila*. *Dev Biol.*

572 Isabella, A.J., and Horne-Badovinac, S. (2016). Rab10-Mediated Secretion Synergizes
 573 with Tissue Movement to Build a Polarized Basement Membrane Architecture for Organ
 574 Morphogenesis. *Dev Cell* 38, 47–60.

575 Kaushik, S., Pickup, M.W., and Weaver, V.M. (2016). From transformation to
 576 metastasis: deconstructing the extracellular matrix in breast cancer. *Cancer Metastasis*
 577 Rev 1–13.

578 Lewellyn, L., Cetera, M., and Horne-Badovinac, S. (2013). Misshapen decreases
 579 integrin levels to promote epithelial motility and planar polarity in *Drosophila*. *J. Cell Biol.*
 580 200, 721–729.

581 Lipari, K.R., Chen, D.-Y., Deghan, Y., Streichan, S., and Bilder, D. (2016). Symmetry-
 582 breaking in an edgeless epithelium by Fat2-regulated MT polarity. *Cell Reports*.

583 Maggert, K.A., Gong, W.J., and Golic, K.G. (2008). Methods for homologous
 584 recombination in *Drosophila*. *Methods Mol. Biol.* 420, 155–174.

585 Martinek, N., Shahab, J., Saathoff, M., and Ringuette, M. (2008). Haemocyte-derived
586 SPARC is required for collagen-IV-dependent stability of basal laminae in *Drosophila*
587 embryos. *Journal of Cell Science*.

588 Morrissey, M.A., and Sherwood, D.R. (2015). An active role for basement membrane
589 assembly and modification in tissue sculpting. *Journal of Cell Science* 128, 1661–1668.

590 Munjal, A., Philippe, J.-M., Munro, E., and Lecuit, T. (2015). A self-organized
591 biomechanical network drives shape changes during tissue morphogenesis. *Nature*
592 524, 351–355.

593 Pastor-Pareja, J.C., and Xu, T. (2011). Shaping cells and organs in *Drosophila* by
594 opposing roles of fat body-secreted Collagen IV and perlecan. *Dev Cell* 21, 245–256.

595 Rauzi, M., Verant, P., Lecuit, T., and Lenne, P.-F. (2008). Nature and anisotropy of
596 cortical forces orienting *Drosophila* tissue morphogenesis. *Nat. Cell Biol.* 10, 1401–
597 1410.

598 ray, R.P., Matamoro-Vidal, A., Ribeiro, P.S., Tapon, N., Houle, D., Salazar-Ciudad, I.,
599 and Thompson, B.J. (2015). Patterned Anchorage to the Apical Extracellular Matrix
600 Defines Tissue Shape in the Developing Appendages of *Drosophila*. *Dev Cell* 34, 310–
601 322.

602 Rosenbluth, M.J., Lam, W.A., and Fletcher, D.A. (2006). Force microscopy of
603 nonadherent cells: a comparison of leukemia cell deformability. *Biophys. J.* 90, 2994–
604 3003.

605 Sarov, M., Barz, C., Jambor, H., Hein, M.Y., Schmied, C., Suchold, D., Stender, B.,
606 Janosch, S., Kj, V.V., Krishnan, R.T., et al. (2016). A genome-wide resource for the
607 analysis of protein localisation in *Drosophila*. *eLife* 5.

608 Schindelin, J., Arganda-Carreras, I., Frise, E., Kaynig, V., Longair, M., Pietzsch, T.,
609 Preibisch, S., Rueden, C., Saalfeld, S., Schmid, B., et al. (2012). Fiji: an open-source
610 platform for biological-image analysis. *Nat. Methods* 9, 676–682.

611 Shyer, A.E., Tallinen, T., Nerurkar, N.L., Wei, Z., Gil, E.S., Kaplan, D.L., Tabin, C.J.,
612 and Mahadevan, L. (2013). Villification: How the Gut Gets Its Villi. *Science* 342, 212–
613 218.

614 Spradling, A.C. (1993). Developmental genetics of oogenesis. In *The Development of*
615 *Drosophila Melanogaster*, M. Bate, and A. Martinez Arias, eds. (New York: CSHL
616 Press), pp. 1–70.

617 Thompson, D.W. (1917). *On Growth and Form* (Cambridge University Press).

618 Tucker, J.B., and Meats, M. (1976). Microtubules and control of insect egg shape. *J.*
619 *Cell Biol.* 71, 207–217.

620 Van De Bor, V., Zimniak, G., Papone, L., Cerezo, D., Malbouyres, M., Juan, T.,
621 Ruggiero, F., and Noselli, S. (2015). Companion Blood Cells Control Ovarian Stem Cell
622 Niche Microenvironment and Homeostasis. *Cell Reports* 13, 546–560.

623 Varner, V.D., and Nelson, C.M. (2014). Cellular and physical mechanisms of branching
624 morphogenesis. *Development* 141, 2750–2759.

625 Vichas, A., and Zallen, J.A. (2011). Translating cell polarity into tissue elongation.
626 *Semin Cell Dev Biol.*

627 Viktorinova, I., Konig, T., Schlichting, K., and Dahmann, C. (2009). The cadherin Fat2 is
628 required for planar cell polarity in the *Drosophila* ovary. *Development* 136, 4123–4132.

629 Viktorinová, I., and Dahmann, C. (2013). Microtubule polarity predicts direction of egg
630 chamber rotation in *Drosophila*. *Current Biology* 23, 1472–1477.

631 Walck-Shannon, E., and Hardin, J. (2014). Cell intercalation from top to bottom. *Nature*
632 *Reviews Molecular Cell Biology* 15, 34–48.

633 Went, D.F., and Junquera, P. (1981). Embryonic development of insect eggs formed
634 without follicular epithelium. *Dev. Biol.* 86, 100–110.

635 Xi, R., McGregor, J.R., and Harrison, D.A. (2003). A gradient of JAK pathway activity
636 patterns the anterior-posterior axis of the follicular epithelium. *Dev Cell* 4, 167–177.

637

FIGURE LEGENDS

Figure 1. A mechanical stiffness gradient in the follicle basement membrane.

(A) Elongation of the *Drosophila* follicle during oogenesis involves three components: the luminal germline, a surrounding epithelium, and an encasing basement membrane (BM) (See also Figure **Supplement 1**). Aspect ratios of st. 3, 5, and 7 egg chambers stained for DAPI (blue) and phalloidin (red), along with CollIV-GFP (green), are shown. (B) Atomic Force Microscopy (AFM) measurement of BM stiffness in living follicles. Absence of stroma and external position of BM allows direct access of AFM probe. (C) Follicles are probed at different regions along the A-P axis, including the poles via PDMS 'egg cartons'. Stiffness measurements are derived from the first 50 nm of force-extension curves. (D) BM stiffness in the follicle center increases during development. Collagen digestion but not F-actin network disruption eliminates nearly all AFM-measured stiffness. (cf **Supplement 1**) (E) Regional BM stiffness along the follicle A-P axis; color intensity matches position as in C. WT follicles develop an A-P symmetrical gradient of mechanical anisotropy. Anterior and posterior poles are not distinguished. (F) *fat2* and *msn*-depleted follicle BMs do not increase stiffness during development, and remain mechanically isotropic. Scale bar: 25µm.

Figure 2. Manipulating the BM stiffness gradient alters organ shape.

For each follicle genotype, AFM-measured positional stiffness at st. 7-8 is shown above and degree of elongation is shown below. Manipulations in **A-F** alter gene expression uniformly via *tjGAL4* (**I**) or homozygous genotype, while **G-H** alter gene expression regionally using centrally-expressed *mirGAL4* or terminally-expressed *fruGAL4* (**J, K**). Compared to WT (**A**), depletion of SPARC (**B**) softens the BM but preserves the anisotropic gradient; follicles elongate comparable to WT. Depletion of Col IV throughout the epithelium (**C**) creates a uniformly soft follicle with severe elongation defects, resembling *fat2* mutants or depletion of *msn* (**D, E**). EHBP1 overexpression (**F**) increases stiffness while retaining an anisotropic gradient, and follicles hyperelongate. Depletion of Col IV in the central region alone (**G**) flattens the gradient while leaving terminal stiffness intact; this results in elongation defects. EHBP1 overexpression in the terminal regions alone (**H**) also flattens the gradient and results in elongation defects. **L** charts aspect ratio vs stiffness anisotropy (defined as the ratio of central stiffness to the mean stiffness throughout the AP axis) for genotypes **A-H**; also included are *tj>Dome^{DN}* (**6J, K**) and *tj>Perl^{OE}* (**5H, I**).

Figure 3. The BM stiffness gradient creates anisotropic resistance to organ expansion.

(A) Design of osmotic swelling experiments. Immersion in water causes influx (blue arrow) into the follicle (diagrammed in cross-section), resulting in increased turgor pressure (red arrows) that is resisted by BM (green) as the organ swells. (B) WT follicle expressing CollIV-GFP, 1' and 24' after immersion (cf **Video 1**). Position of BM breach is indicated by arrowhead. (C) Frequency of follicle BM failure by stage and genotype, along with timing (D) of failure. WT BMs accommodate expansion with increasing efficiency as development proceeds in a manner independent of cellular F-actin; *fat2* and collagenased follicles burst frequently and rapidly. (E) Position of BM failure: WT BMs breach most frequently at poles whereas *fat2* and collagenased follicles also breach in other regions. (F) Frequency of BM failure in manipulated st. 7-8 follicles and (G) aspect ratio immediately before bursting. Scale bar: 25µm.

Figure 4. Uniform circumferential mechanics in elongating follicles.

(A) 'Unrolling' of organ surface by ImSAnE allows quantitation of BM components along both AP and circumferential axes. Image taken from Chen et al., 2016. (B) Analysis of BM fibril PCP shows WT polarity when *Perl* or *Dome*^{DN} are overexpressed, or when SPARC is depleted, contrasting with altered polarity in *fat2* and absence in *Col IV* depletion. (C, D) Unrolling reveals increased variance in circumferential *Col IV* levels in *fat2* as compared to WT or *Perl*-overexpressing follicles. Heat map indicates lowest (blue) to highest (red) intensities over equivalent ~35% circumferential segments. (E, F) AFM analysis along the circumferential axis of a follicle at a single central meridian. *fat2* follicles show high variability in BM stiffness, compared to the consistent values of WT or *Perl*-overexpressing follicles. Scale bars: 5µm and 10µm, respectively.

Figure 5. Morphogen-like signaling creates the stiffness gradient.

Expression of GFP protein traps in BM components, assessed in WT st. 7-8 follicles, physically flattened for visualization: (A) CollIV, (B) Laminin B1, (C) Perlecan. Heat map indicates lowest (blue) to highest (red) intensities. The A-P CollIV pattern is disrupted in st. 7-8 follicles mutant for *fat2* (D, cf **Supplement 1**) or with inhibited JAK/STAT signaling (*tj>dome*^{DN}, E) (cf **Supplement 2**). (F) *Col IV* transcription (*CollIV-LacZ* reporter expression) is not elevated in the central follicle; (G) uniform production of CollIV (via *hsFLP; act>y+>GAL4 UAS-myr-RFP*) throughout the follicle (G') results in elevated central incorporation. (H) ImSAnE 'unrolling' of CollIV-GFP expressing follicle surface allows quantitation of intensity along the entire A-P axis; note the shorter axis of 'round' genotypes. (I) Along the A-P axis, CollIV levels are significantly elevated in the central region of WT and *Perl*-overexpressing but not *fat2* or *dome*^{DN}-expressing follicles. (J) Elongation failure induced by inhibition of JAK-STAT signaling or overexpression of *Perl* in follicles (K). AFM reveals that follicles with inhibited JAK-STAT signaling or *Perl* overexpression do not develop an A-P stiffness gradient; *Perl* overexpressing follicles are softer than WT. (L) *Perl*-overexpressing follicles burst

easily under osmotic challenge, whereas follicles with inhibited JAK-STAT signaling are more similar to WT. Scale bars: 25µm and 10µm, respectively.

Video 1: WT Follicle swelling in H₂O. Bursting of WT follicles when placed in water as shown in **Figure 4B**. Follicle nuclei are visualized using Histone-mRFP, and BM is labeled with CollIV-GFP fluorescence (green).

Video 2: *fat2* follicle swelling in H₂O. Rapid bursting of *fat2* follicles when placed in water as quantified in **Figure 4D**. Follicle is visualized using FM4-64, and BM is labeled with CollIV-GFP fluorescence (green).

Video 3: Follicle rotation in manipulated genotypes. Rotation of *tj>Perl* and *tj>Dome-DN* is comparable to WT, while *tj>abi-RNAi* initiated at st. 5 blocks rotation. Scale bar: 10µm.

Video 4: Osmotic bursting of manipulated genotypes placed into water. As quantified in **Figure 4E-G**, Compared to WT, *fat2* follicles burst rapidly and often not at poles, while follicles uniformly overexpressing EHBP1 (*tj>EHBP1*) swell anisotropically and do not burst at all. Overexpressing EHBP1 in poles (*fru>EHBP1*) induces generally isotropic swelling but also prevents bursting. Depleting Coll IV in the central region (*mirr>Col IV KD*) cause isotropic swelling and central bursting.

SUPPLEMENTARY MATERIAL

Figure 1 – Figure Supplement 1: Isotropic mechanical properties of cells in the *Drosophila* ovary. (A-B) Cross-section of the acinus-like *Drosophila* follicle; planar epithelial and luminal expansionary forces, as well as basement membrane-based resistance, are diagrammed. (C-E) As compared to elongation of growing WT follicles (C), growth of follicles following ablation of epithelium (*tjGAL4 GAL80ts>Diphtheria toxin*

A chain, **D**) is isotropic. Note absence of epithelium-produced BM (inset). Aspect ratio is quantitated in **E**. **(F)** Assessment of cortical tension in follicle epithelial cells using laser nanodissection (red) and Myo:GFP localization (blue). **(G)** Severing of AP and circumferential cell junctions at anterior, center, and posterior positions results in comparable recoil velocities. Example AP and Circ. Cuts in G' and G". **(H)** Junctional non-muscle MyoII (Myo:GFP) localization is equivalent along A-P and circumferential cell junctions. Representative example in H'. Scale bars: 25µm in A-C, 5µm inset in G'-H'.

Figure 1 – Figure Supplement 2: AFM elasticity measurement method. (A) Follicles are indented to generate extension-deflection curves. Only the first 50nm of deflection (plus 50nm pre-contact) are used to fit for the Young's modulus. Four curves are generated per position, averaged, then compared between A-P positions. (B) Indentation piezo (extension) speed optimization. Reduced stiffness at high speeds (0.8-1.0µm/s) are indicative of viscoelasticity. 0.4µm/s provided optimal elasticity accuracy and measurement speed.

Figure 1 – Figure Supplement 3: Validation of pharmacological and hypertonic shock treatments for BM stiffness. (A) Collagenase treatment of follicles prior to AFM does not disrupt cell-cell junctions, as monitored by E-cadherin-GFP. (B) Latrunculin A treatment of follicles prior to AFM effectively displaces Myo:GFP. (C) Hypertonic shrinkage of WT stage 7-8 follicles causes a significant reduction in size, but no significant loss of BM stiffness. Scale bar: 20µm.

Figure 5 – Figure Supplement 1: *fat2*^{KO} phenocopies other *fat2* null alleles. Loss of basal actin PCP (A), elongation defects (B), Collagen IV-GFP pattern (C, compare to **Figure 6D**) and bursting frequency in distilled water (D) are indistinguishable between *fat2*^{KO} and the well-characterized EMS-generated null allele *fat2*^{58D}. Scale bars: 10µm (A) and 20µm (C).

Figure 5 – Figure Supplement 2: STAT reporter in *fat2* mutants. (A) *fat2* loss does not disrupt A-P patterning, detected by the 10XSTAT-GFP reporter. Scale bar: 20µm.

780

781 **Figure 5 – Figure Supplement 3: BM stiffness and active follicle rotation.**

782 Depletion of actin regulator Abi following st. 5 halts rotation **(A)** but does not soften BM
783 at st. 7-8 **(B)** nor alter bursting characteristics at st. 7-8 **(C)**; follicles show normal
784 elongation at st. 7-8 **(D)** (cf Cetera et al. 2015).

785

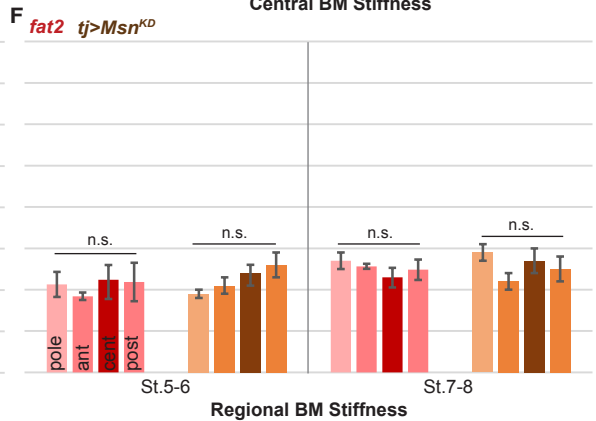
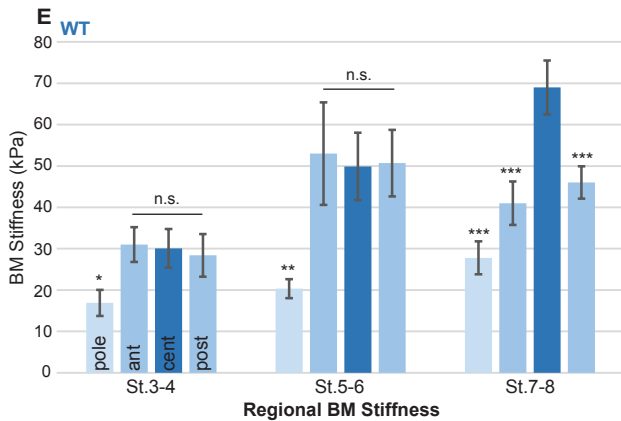
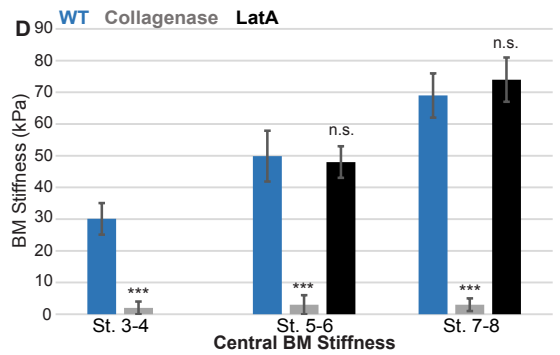
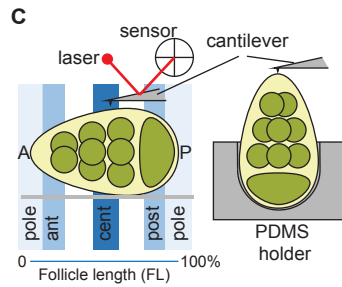
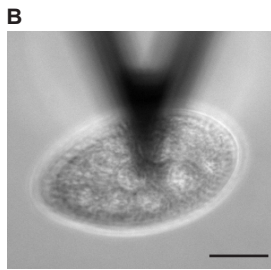
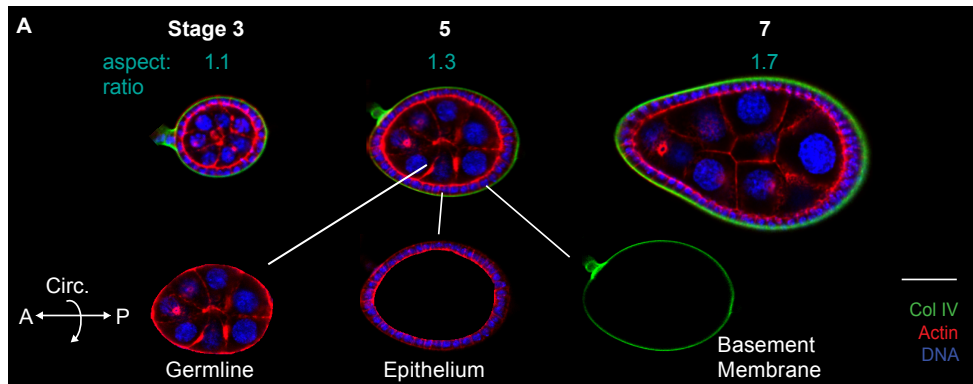
786 **Supplementary Table 1.** Experimental Genotypes.

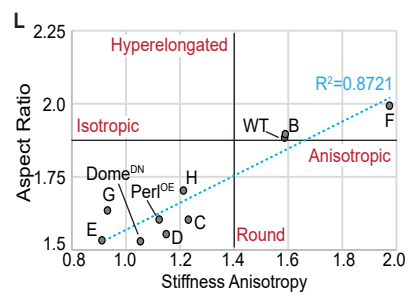
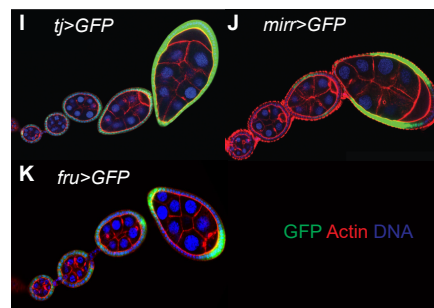
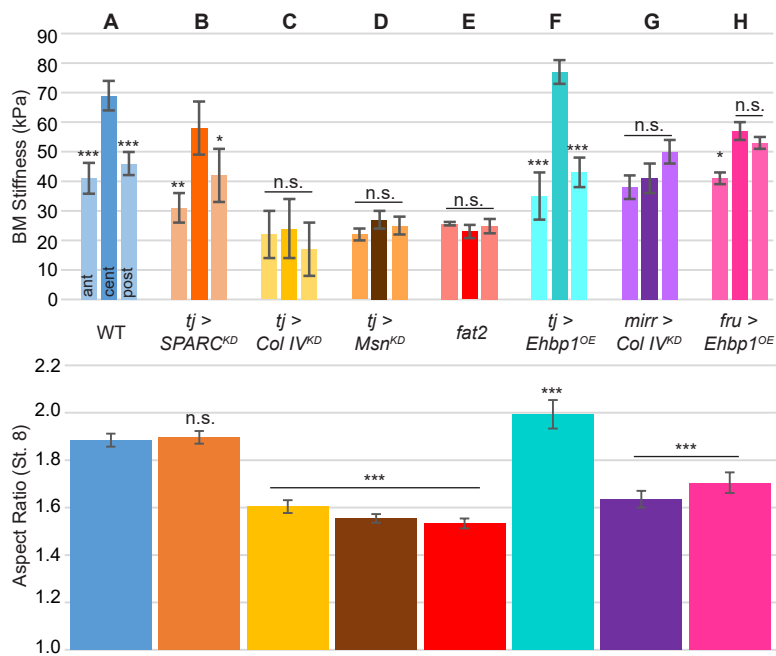
787 **Source code File 1.** AFM Curve Fitting.

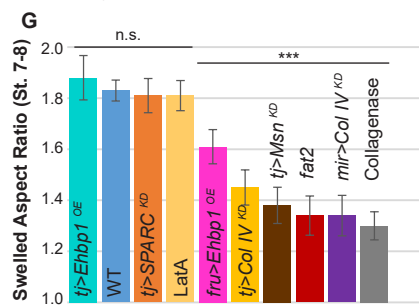
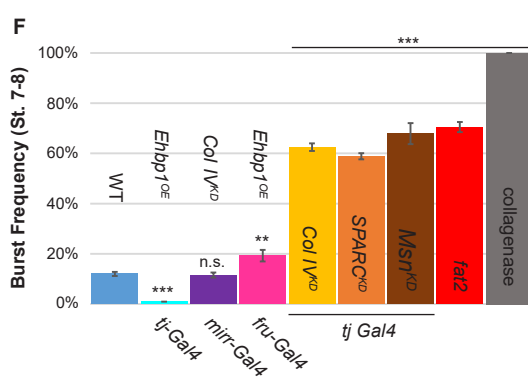
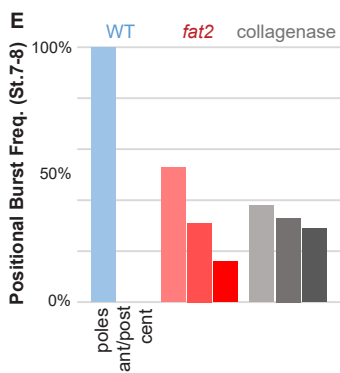
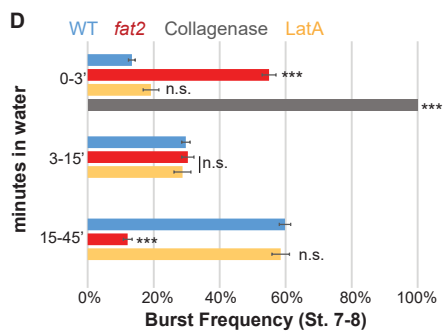
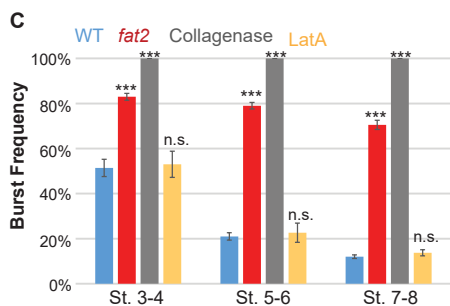
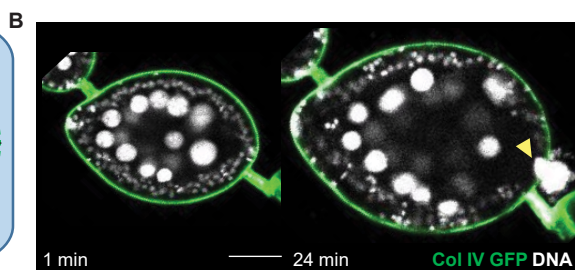
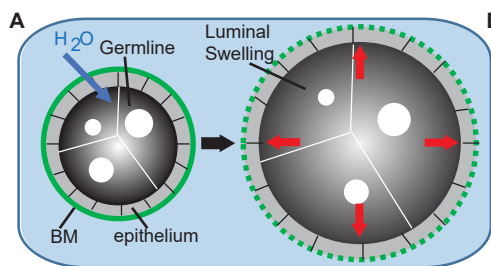
788

789

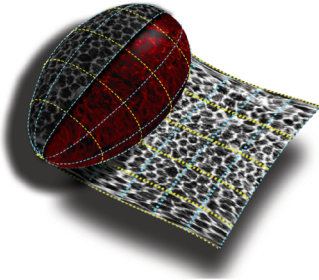
790



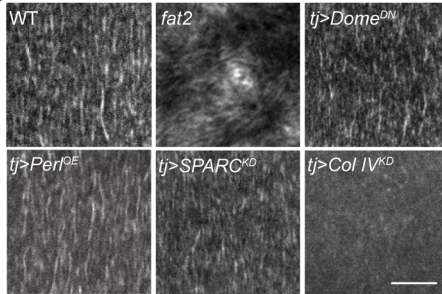




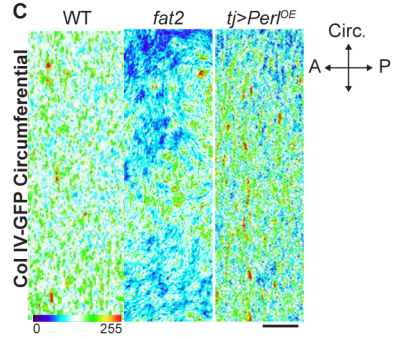
A



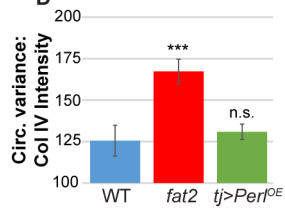
B



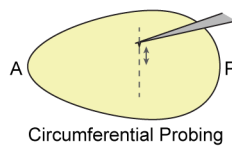
C



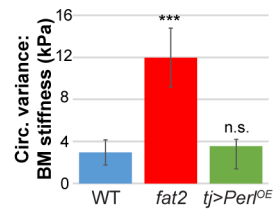
D

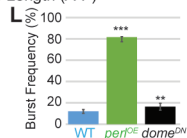
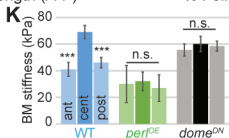
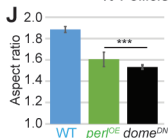
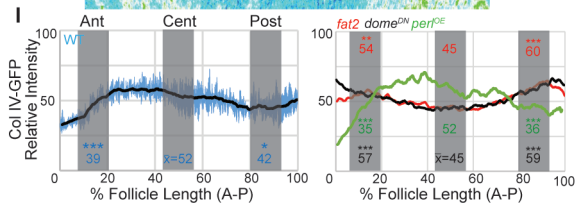
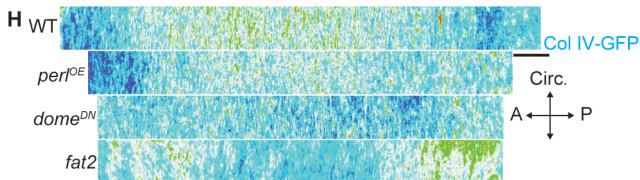
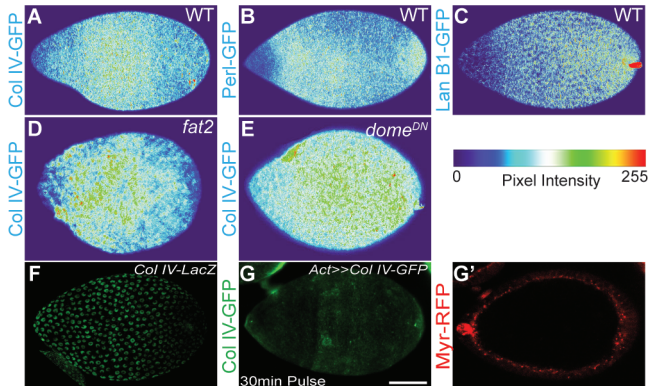


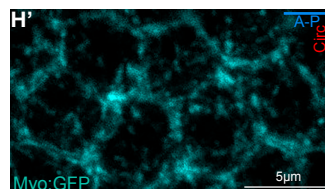
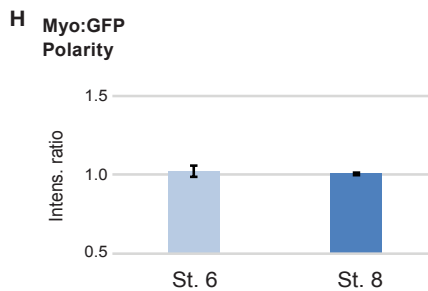
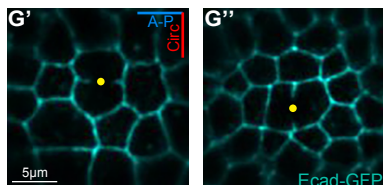
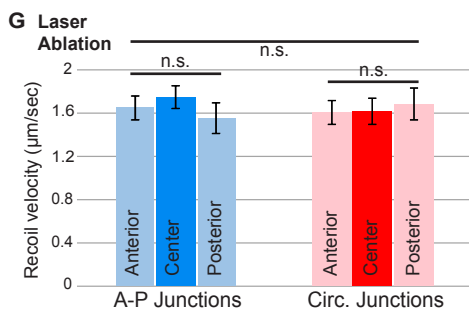
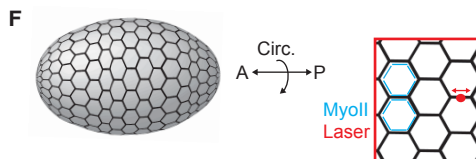
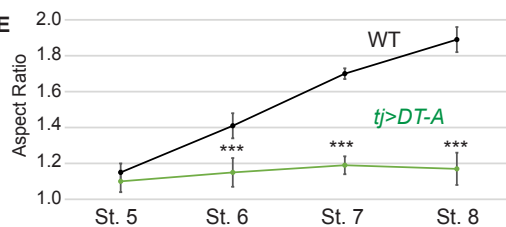
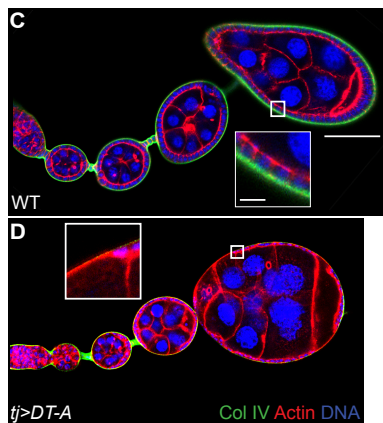
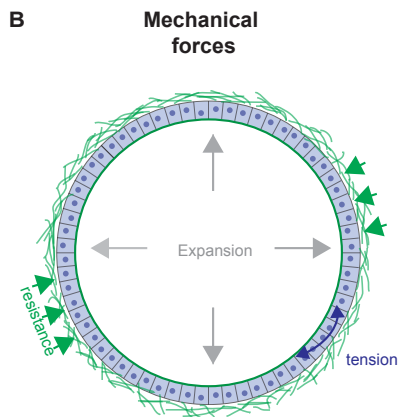
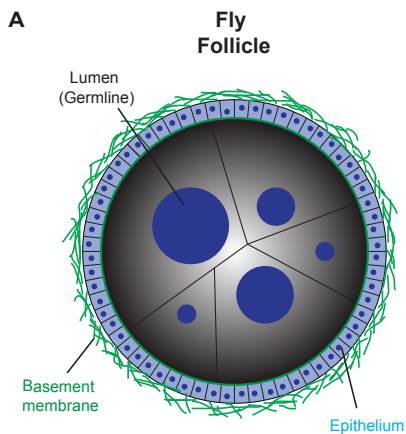
E

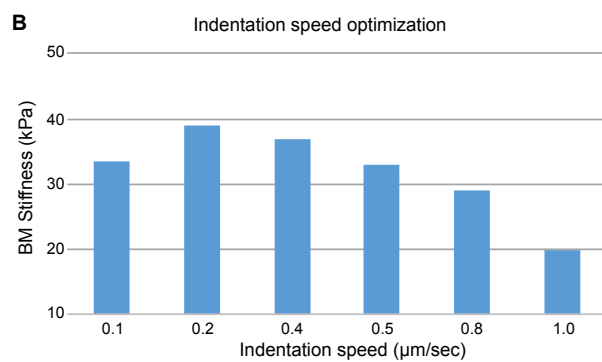
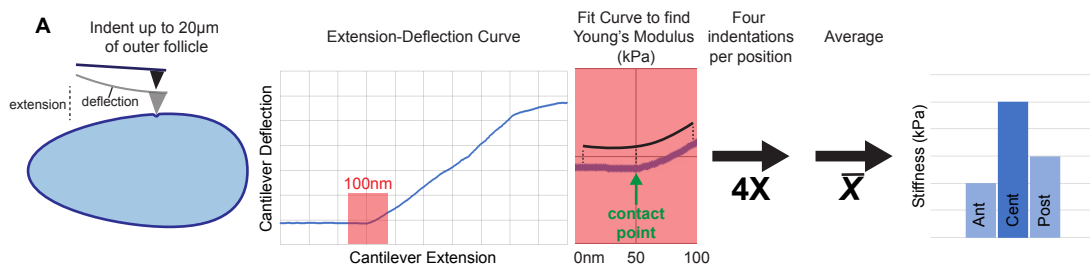


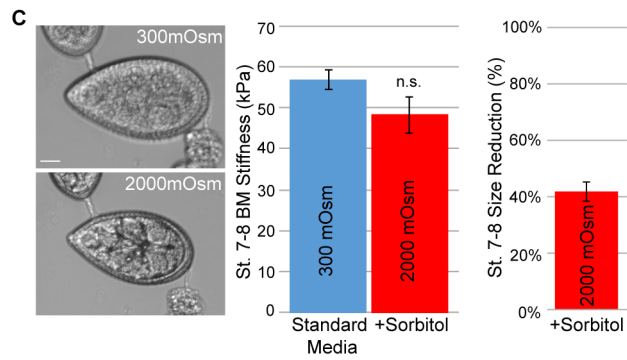
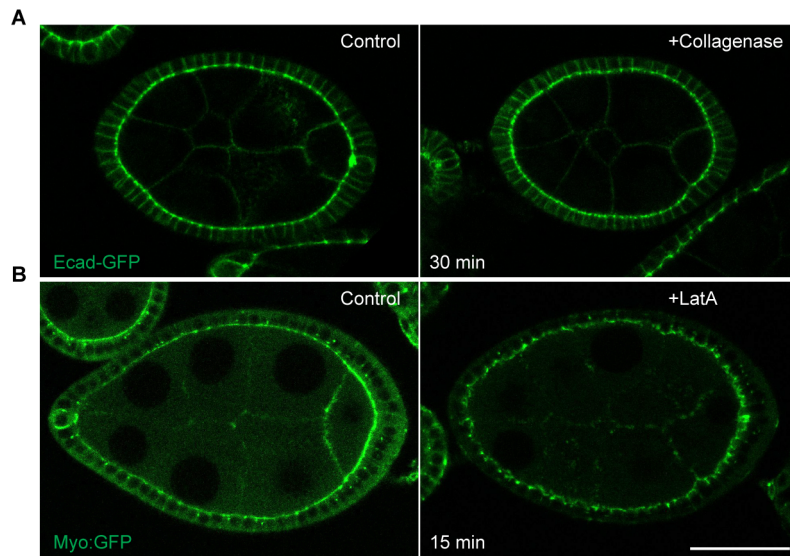
F

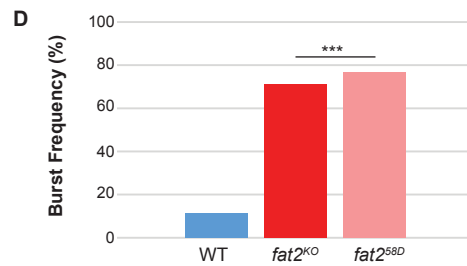
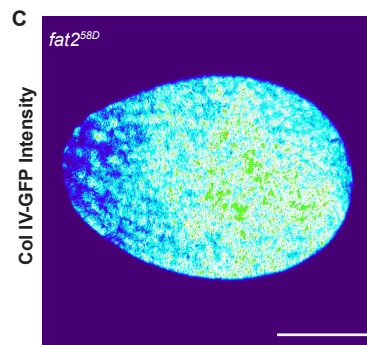
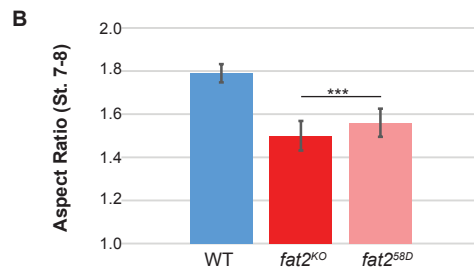
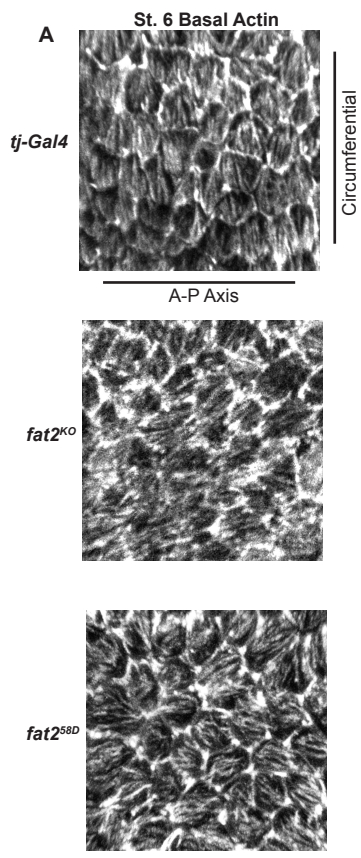












A

